Application of a generalized diffraction analysis to the design of nonstandard Lyot-stop systems for earth limb viewing radiometers

Martin E. Caldwell, MEMBER SPIE
Peter F. Gray, MEMBER SPIE
Optical Systems Group
Space Science Department
Rutherford Appleton Laboratory
Chilton, Didcot
Oxfordshire OX11 OQX, United Kingdom
E-mail: m.caldwell@rl.ac.uk

Abstract. The design of Lyot-stop systems in earth limb viewing radiometers is first reviewed, with particular reference to the stray-light analysis methods used for instrument design and performance evaluation. These methods are given in order of increasing sophistication, up to the most powerful technique for diffraction analysis, that of generalized beam propagation analysis. The typical design features of radiometers for the limb-viewing application are discussed to summarize the important stray-light issues, including scatter, ghosting, and diffraction effects. How for multichannel instruments based on arrays of detectors, the interplay of these issues affects the Lyot-stop system is shown, pushing the design toward nonstandard geometries for which the generalized analysis method becomes essential. An example is given of the use of the technique in a system requiring a nonstandard Lyot-stop geometry, including the computation of the full diffracted energy patterns at each stage of the Lyot-stop system, illustrating the physics of the diffraction suppression, and giving insight into the design trade-offs; in particular, that between signal throughput and diffraction rejection. For one choice of this trade-off, the net diffraction response is calculated. This quantity is an important input to the ground characterization of the predicted performance.
[S0091-3286(97)02610-X]

Subject terms: stray light; diffraction; Lyot stop; earth limb viewing; radiometer.

Paper 29027 received Feb. 23, 1997; revised manuscript received May 23, 1997; accepted for publication May 23, 1997.

1 Introduction

Many challenging optical engineering problems involve the detection of a faint object in close proximity to a much brighter object. Examples include the imaging of the sun's corona,[1] and more recently, the detection of extra-solar-system planets around stars,[2] and the detection from space of the earth atmosphere radiance close to the earth's limb.[3]

In such systems, although the brighter object is outside of the telescope field of view, energy from it is diffracted at the entrance aperture, through sufficient angle to enable it to enter the field of view. Because the off-axis object is much brighter than the object being viewed, its diffracted energy may obscure the wanted faint object signal.

The Lyot stop was invented to overcome this problem in the case of viewing of the sun's corona.[1] It is a stop placed at the image of the diffracting entrance aperture, where the diffracted rays are refocused near the image of the entrance aperture edge. A small undersizing of the Lyot stop with respect to the entrance aperture's image can then efficiently block the brighter diffracted rays, removing much of the unwanted light. A description of the Lyot-stop process is given in Sec. 2.

The Lyot stop has become an important design feature of radiometers that view the earth's limb from space.[4–8] Here the wanted faint signal is typically a narrow-band IR thermal emission from trace gases in the atmosphere, and the unwanted bright off-axis source is the broadband thermally radiating earth, with the earth's horizon typically lying very close (<1 deg) to the edge of the field of view. In such cases, the diffraction and scatter lead to the earth producing an unwanted background signal on the radiometer detectors, and this is termed the nonrejected earth radiance[9] (NRER). This parameter is often the largest background, which limits the measurement accuracy, and so it is a major driver in instrument design. To meet the measurement requirements, modern IR telescopes are designed as high stray-light-rejection systems,[3] whose key features can include

1. multiple Lyot-stop stages
2. all-reflective, off-axis mirror systems with unobscured aperture, to minimize diffraction
3. high-quality mirrors, of the best achievable cleanliness, to minimize incoherent scatter.

Even with these precautions, the fundamental limits on diffraction and optical component quality mean that the NRER remains a significant quantity, which must be predicted and confirmed prior to launch[4] to ensure maximum sensitivity in the science mission.

Here, we first give a physical description of the Lyot-stop operation (Sec. 2), and this is used to review the pre-

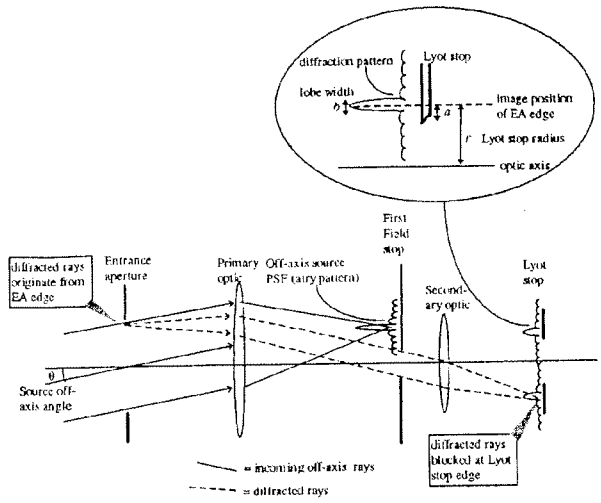

Fig. 1 Schematic of Lyot-stop optical system consisting of diffracting entrance aperture, primary optic, field stop, secondary optic, and Lyot stop at the entrance aperture (EA) image. Incoming off-axis rays and diffracted rays are shown.

vious analysis methods as applied to various instruments of this type. The review illustrates the increasing complexity of both the sensor hardware, and the stray-light-analysis tools used for design and characterization.

In Sec. 3, we review the typical design features of limb-viewing instruments, in which the diffracted stray-light issue and its defense become especially important for the following reasons:

1. Relatively long wavelengths (up to 17 μm) and low viewing altitudes (0.2 deg from the earth disk) are involved.
2. The use of aperture sharing in instruments with multiple detection paths and/or multiple wavelength channels complicates the stray-light design, introducing the possibility for channel crosstalk via ghost and scatter effects. The presence of apertures to suppress these complicates the design for diffraction defense, leading to nonstandard Lyot-stop systems.
3. High spatial resolution is required in the vertical direction (altitude) as a main science goal. To achieve this, the stray-light-limited response function of the instrument must be optimized and accurately known.

After explaining how these features lead to the requirement for a generalized diffraction analysis, in Sec. 4 we demonstrate the application of the Gaussian beam superposition method to an example system. This shows how the technique, implemented in a ray-trace program, is able to accurately compute the optical diffracted energy patterns throughout the system, as required for the design trade-off and performance studies.

2 Review of Lyot-Stop Diffraction Analyses

2.1 *Physical Description*

The Lyot-stop process is described using Figs. 1 to 4, which are for a generalized optical system. In Fig. 1, light from a distant point source is incident on the system as a plane wavefront at an off-axis angle of θ. Here by stray light we mean light from off-axis angles that are outside of the instrument field of view, and this is referred to here as "out-of-field" light. The out-of-field light at angle θ is focused to a point on the first image plane, where it is blocked by the first field stop. It is also diffracted at the circular EA, producing an Airy ring pattern that extends across the field stop, so that some diffracted light is transmitted through the stop. In the boundary-wave formulation,[10,11] this diffracted energy is represented by rays emanating from the aperture rim, as shown by the dashed lines in the figure. At the subsequent pupil plane (the image of the EA), the diffracted rays are refocused to produce a bright ring in a position corresponding to the geometrical image of the EA edge. The Lyot stop is positioned at this image and is made smaller than the geometrical image of the aperture so that the bright ring is blocked, as shown in the diagram, and most of the diffracted light is thereby eliminated.

In imaging the diffracted rays through the field stop, the width of the bright ring (dimension b in the insert to Fig. 1) is determined by the size of the field stop, as this limits the angular range of the diffracted rays that are imaged. In the diffraction-limited case, the width b of the ring is given by the f-number F of the cone of diffracted rays at the Lyot stop. For circular stops, the relation is that of the Airy disk diameter[12]:

$$b = 2.44\lambda F. \tag{1}$$

However much of the diffraction pattern is blocked by the undersizing of the Lyot stop, part of it corresponding to higher diffraction angles will always leak past the stop, as shown in the insert in Fig. 1. The degree of blocking actually achieved by the Lyot-stop system is described in terms of the diffraction reduction ratio R, and this is defined as the ratio of the diffracted energy that reaches the detector, with the stop present, to that without the stop.[13] Note that R is a function mainly of the diffraction image width b and the undersize dimension of the stop relative to the bright ring image, dimension a in the figure. Normally both a and b are small relative to the Lyot-stop radius r, and efficient blocking to $R<1\%$ can be obtained for a small undersize factor $a/r<5\%$. Such an arrangement, where the main bright diffraction ring is efficiently blocked, is a defining feature of systems described as "well baffled" in the stray-light literature.[14,15]

For the stray light leaked past the Lyot stop, the subsequent imaging to the detector plane is also important, and this part of the analysis is shown in Fig. 2(a). In the absence of the Lyot stop, the pattern at the detector plane would be simply the image of that at the first image plane. When the Lyot stop is present, the manner in which it blocks the main diffraction ring can be thought of as a spatial filtering action. The residual light, when propagated on to the second field stop, is found to be concentrated around the image of the first field stop edge, and in the boundary wave formulation, it can be attributed to diffracted rays from the first field stop edge, drawn as dotted lines in Fig. 2(a). Thus, for a well-baffled Lyot-stop system, the residual light at the

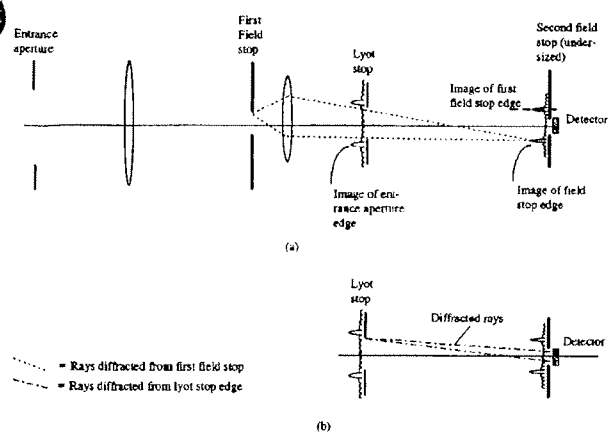

Fig. 2 Optical system of Fig. 1 showing rays diffracted from subsequent apertures.

second field stop is mainly due to diffraction from the first field stop edge, and so the pair of conjugate planes formed by the field stops has a similar diffraction relationship to that between the entrance aperture and the Lyot stop. The diffracted stray light can therefore be further reduced by undersizing the second field stop with respect to the first, as shown in the figure, and a typical Lyot-stop system involves undersizing of both the pupil-plane and the image-plane stops with respect to the images of the preceding stops. In systems with multiple imaging stages, a number of Lyot-stop stages can be implemented, and the repeated undersizing of the stops in such cases has been referred to[5] as a "cascaded stop design."

In the field stop diffraction, as in the EA diffraction, there is finite resolution in the imaging of the diffraction pattern. Consequently some of the diffracted energy extends across the undersized second field stop [Fig. 2(a)], and if the detector is positioned at this plane, this constitutes the residual level of diffracted stray light, which is finally measured. If there were subsequent onward imaging, an analysis at the next pupil plane would reveal that this detected energy originated mainly by diffraction from the Lyot-stop edge, and the corresponding diffracted rays are shown in Fig. 2(b).

The diffracted ray picture of Figs. 1 and 2 can be combined, as shown in Fig. 3, to describe the whole Lyot-stop process in terms of multiple diffractions, where the following nomenclature is used:

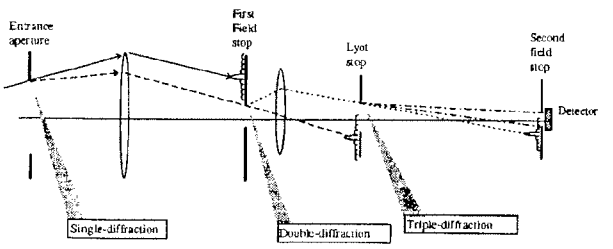

Fig. 3 Three levels of diffraction in the Lyot-stop system (summary of Figs. 1 and 2).

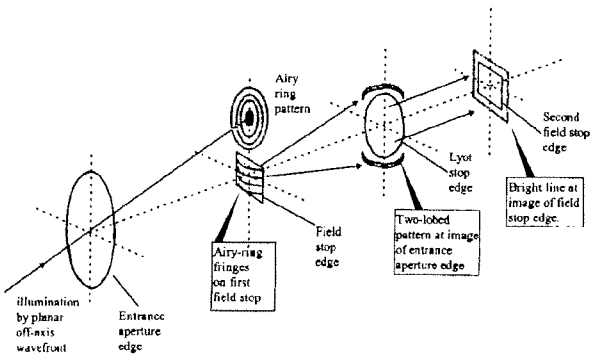

Fig. 4 Schematic showing apertures and diffraction patterns of Figs. 1 and 2 in two dimensions.

1. For the out-of-field incident beam, the "undiffracted" rays are blocked at the first field stop.
2. Out-of-field rays undergo "single diffraction" (at the EA only) but are blocked at the Lyot stop.
3. Out-of-field rays undergo "double diffraction" (at the EA and the field stop) but are blocked at the second field stop.
4. Out-of-field rays undergo "triple diffraction" (at the EA, the field stop, and the Lyot stop) and reach the detector.

In this way, the residual energy at the detector in a well-baffled Lyot-stop system has been called the triple-diffraction term.[15]

Figure 4 illustrates how the energy patterns drawn in section in Figs. 1 and 2, would appear in two dimensions. In the imaging system described, where all planes of interest are either pupil or image planes and where illumination from a single point source is to be considered, the techniques of Fourier optics can be applied[16] and can be used to determine the optical signal at the consecutive stop planes. The diffraction pattern at the first field stop is then the Fourier transform (FT) of the entrance pupil energy, and for an ideal, circularly symmetric system illuminated by a plane wavefront, this gives the off-axis Airy-ring pattern shown. (More generally, the pattern is the point spread function of the system). This pattern is then spatially filtered by the first field stop and Fourier transformed to produce the pattern at the Lyot stop. In Fig. 4, because the source is off axis in the vertical direction, the Airy rings produce largely horizontal fringes within the field stop. Consequently, at the Lyot stop, the energy pattern is dominated by lobes at the upper and lower sides of the stop, as shown.*

In the absence of blocking by a Lyot stop, the light would propagate on to the second field stop to produce a straightforward image of the pattern at the first field stop. With Lyot-stop blocking, however, the spatial filtering of the two-lobed pattern produces a pattern at the second field

*In the classical Lyot stop for solar observation, the unwanted source is at the center of the field of view, and the field stop in this case is in the form of a central obscuration. The stray light is circularly symmetric, made up of equal components in all directions, and so the two-lobed pattern of Fig. 4 would "fill out" to become a complete, axially symmetric ring.

stop that is dominated by a bright line, this being an image formed by light diffracting from the edge of the first field stop, as explained earlier.

2.2 *Review of Analysis Methods*

The aim of most analyses is to find, for a given geometry and illumination, the amount of energy from the bright off-axis source that, by diffraction, eventually reaches the detector, thereby contributing to the overall stray-light level.

2.2.1 *Numerical Fourier analysis*

The Fourier optics property suggests a numerical analysis, involving conceptually simple image processing techniques. The diffraction image at each plane is described using an array of pixels, applying a numerical Fourier transform to compute the energy at the next plane. For the first field stop this method is similar to that used to compute the point spread function (PSF) of a system, as the FT of the complex amplitude at the exit pupil.[17] For a circular aperture, neglecting aberrations, the normalized PSF is given by the Airy formula[18]:

$$\mathrm{PSF}=\left[\frac{2J_1(kD\beta/2)}{(kD\beta/2)}\right]^2, \tag{2}$$

where

$$k=2\pi/\lambda, \quad \beta=\sin\theta,$$

D is the diameter of the entrance aperture, and J_1 is the first-order Bessel function. The airy disk angular radius is given by

$$\beta_0=1.22\frac{\lambda}{D}. \tag{3}$$

In the stray-light case, because the source is off axis, the important range is usually $\beta \gg \beta_0$; i.e., only the more outlying "wing" of the PSF must be computed. The intensity of the PSF in this region is typically many orders of magnitude lower than the central PSF peak, and so a large dynamic range is required in the FT computation. Also, the Airy-ring pattern is highly oscillatory; the part that is passed by the field stop gives a fringelike pattern, with period approximately equal to β_0, and the field stop may contain hundreds of fringes. For example, in a limb-viewing radiometer with typical values of $\lambda=10\ \mu$m, $D=0.2$ m, and a field stop size of 1 deg, over 300 fringes are present within the field stop.

The numerical analysis required to accurately model such brightness ranges and fine structure is large. Also, the described analysis is for one out-of-field angle only, and it must be repeated for many angles over the range of the off-axis source. These considerations can make the method impractical in terms of the computation time required. Finally, the result from the numerical FT analysis is less amenable to physical insight than are parametric equations, which can, at least for simplified systems, be derived by analytic methods.

2.2.2 *Analytic methods*

Important analytic solutions to the Lyot-stop problem are due to Noll[13] and later Johnson.[19] To discuss these, we first consider the diffraction signal in the absence of a Lyot stop. In this case, the energy passed by the first field stop is all imaged on to the detector, and so it is sufficient to perform an energy analysis at the first image plane only, involving just the single-diffraction rays of Fig. 3. The instrument's susceptibility to stray light from an off-axis angle β is described by the point source transmittance (PST) function,[15] which is closely related to the diffraction PSF already defined. The function PST(β) is defined as the irradiance produced at the detector by a distant source at off-axis position β, divided by the irradiance incident on the instrument from that source. The PST is related to the PSF [Eq. (2)] by[15]

$$\mathrm{PST}=\frac{\pi}{4}\left(\frac{D}{\lambda F}\right)^2 \mathrm{PSF}, \tag{4}$$

where F is the F-number of the beam at the first field stop.

The diffraction PST function is often compared to the analogous functions that describe scattered stray light. In particular, incoherent surface scatter is usually described using the bidirectional scatter distribution function (BSDF), and for ease of comparison the diffraction PST is cast into an equivalent function, known as the bidirectional diffraction distribution function[15] (BDDF). This is given by

$$\mathrm{BDDF}=\frac{4F^2}{\pi}\mathrm{PST}, \tag{5}$$

with units of inverse steradians.

For stray-light analysis, Eqs. (2) to (5) can be simplified. Since the off-axis angles of interest are large ($\beta \gg \beta_0$), the Bessel function is approximated accordingly, and since the typical detector size is much larger than the spacing between consecutive Airy rings, the function is also averaged over the rings.[15] This simplifies the PST to

$$\mathrm{PST}(\beta)=\frac{\pi}{4F^2}\frac{\lambda}{\pi^3 D\beta^3} \quad \text{for } \beta \gg \beta_0. \tag{6}$$

Here the inverse cube dependence on β represents the envelope of the diffraction pattern "wings," and thus the diffracted light dependence on off-axis angle. In a typical stray-light analysis, the preceding functions are used to initially estimate the size of the diffraction threat.

Noll[13] derives the corresponding analytic equations for the case with the Lyot stop present. Noll finds solutions for the diffraction patterns at each plane in the system, using the Fresnel-Kirchhoff integral, with approximations that are valid for circular apertures and for off-axis angles $\beta \gg \delta$, where δ is the sine of the field stop half-angle. This gives an expression for the residual diffracted energy at the center of the detector in terms of the Lyot-stop size. The result is expressed in terms of the Lyot-stop-blocking ratio R (defined previously in Sec. 1). This relates the diffraction response of the defended system, denoted PST_d, to that of the undefended system, denoted PST_0, as

$$\mathrm{PST}_d=R\mathrm{PST}_0, \tag{7}$$

where

$$R=\frac{2}{[\pi kr\delta(1-\alpha^2)]^2}, \tag{8a}$$

$$\alpha=1-\frac{a}{r}, \tag{8b}$$

and the range of validity is

$$\beta \gg \delta \quad \text{and} \quad \frac{a}{r} \ll 1. \tag{8c}$$

Here the Lyot-stop dimensions a and r are the stop radius and undersize, as given in Fig. 1. The ratio a/r is termed the radius undersize factor, and it is the main design parameter for the Lyot stop, having a typical value in the range $a/r < 5\%$. Ratio R is seen to also depend on the field stop size δ; it decreases with decreasing δ, due to loss of resolution in the imaging of the energy rings at the Lyot stop (Fig. 4), i.e., the increased width b of the energy lobe of Fig. 1.

Noll's equation is adequate for systems in which the first field stop size δ is relatively small compared to the off-axis angles of the bright source. In such cases, the variation of diffracted energy across the first field stop is negligible, and R is found to be independent of β.

In current limb-viewing instruments, there is often a requirement to view as close as possible to the earth horizon. Also, for multiple channels, such instruments may utilize an array of detectors, such that the first field stop covers a "composite" field of view, with the separate channel fields being defined by an array of apertures at the second field stop (Sec. 3). This means the first field stop must be large compared to the field of view of a single detector, and it leads to a typical $\delta \approx 1$ deg. These requirements result in increased importance for the smaller off-axis angles where $\beta \approx \delta$. Also, the variation of the diffracted light level with position across the focal plane becomes important, since the stray light must be calculated at the positions of each detector in the array. Johnson[19] has extended the analysis to include the preceding conditions.

Johnson[19] derives the analytic equations for diffracted energy at each stop and includes the variations with position across the field stop, although in one dimension only, that in the plane of incidence. The restriction to circular stops still applies. The blocking ratio R is derived for the regime $\beta \approx \theta$, giving its variation with β and with position on the second field stop (e.g., detector location in the array). For example, at the center of the second field stop, R is given by

$$R=\frac{\alpha\beta^2}{[2\pi kr\delta(1-\alpha^2)]^2}\left[\frac{1}{(\beta-\delta)^2}+\frac{1}{(\beta+\delta)^2}\right] \quad \text{for } \beta > \delta. \tag{9}$$

The asymptotic increase in R as $\beta \to \delta$ reflects the increasing amount of energy that penetrates the first field stop as the center of the PSF approaches the edge of the field stop.

Johnson's equations are included in the program SOAR® (Ref. 15), used for stray-light analysis of instruments of this type.[20]

2.2.3 *Program for the analysis of diffracted energy*

The main limitation of the analytic methods is the restriction to circularly symmetric systems. For detailed analysis, the full system geometry must be modeled, and for limb-viewing instruments this typically includes the off-axis "z folded" telescope, a field stop that has a rectangular shape to match the earth horizon, and an array format for the detection channels. Diffraction in such complex geometries cannot be described analytically. A numerical method, based on the boundary wave formulation combined with ray tracing, was developed by Greynolds[21] to model diffraction from stop and baffle edges in optical systems of arbitrary complexity.

Here the computational size problem of the Fourier optics method is reduced as follows. First, the problem is cast into the boundary wave formulation, reducing the normal 2-D aperture integral to a 1-D integral around the aperture edge. Second, the stationary phase (SP) approximation is used to show that for well-baffled conditions, the diffraction patterns are dominated by a small number of diffracted ray paths. Tracing of diffracted rays from only these SP points can then adequately describe the diffraction pattern.

The method is implemented in the program for analysis of diffracted energy[21] (PADE). In this program, a full geometric model of the optical system is constructed, and the stray light is calculated in terms of energy transfer between surfaces and edges, by both scatter and diffraction. For the diffraction analysis, this involves finding the SP paths between successive planes, beginning at the first diffracting aperture and ending at the detector. For a Lyot-stop system the resulting SP paths are a subset of the triple-diffraction paths of Fig. 3. These SP paths are ray traced, and at each diffraction stage, a BDDF value is calculated to represent the energy in the diffracted ray. Therefore in the case of triple diffraction there are three BDDFs involved, and these are multiplied together to find the residual energy at the detector. This reduction of the problem to only SP rays greatly reduces the computation required, and this becomes crucial to analysis of systems that are complex or which require a wide range of off-axis angles to be analyzed.

As well as enabling real geometries to be included, the PADE program also enables aberration effects to be incorporated, via numerical ray tracing as in standard optical design software. In addition, the BDDF can be calculated for near-field (Fresnel) as well as far-field (Fraunhoffer) diffraction, and this means that stops that are not at pupil or image planes could also be analyzed.

For the application to be presented here, the main restriction of the method is that the far-field BDDF is valid only for diffraction angles greater than the Airy disk radius, as in Eq. (6). This means the method cannot be used to compute the main lobes of the diffraction pattern at each stop, and so as in the analytic techniques, it is restricted to well-baffled systems in which these lobes are all efficiently blocked by the stops (e.g., Fig. 3). This restriction is acceptable for instruments where a high degree of Lyot-stop rejection is implemented, and the cryogenic limb array étalon spectrometer (CLAES) instrument is an example where

PADE has been used to analyze a well-baffled system with two Lyot-stop stages.[5]

2.2.4 *Beam propagation methods*

These methods are related to those of Sec. 2.2.1, where the image plane diffraction pattern was given by the PSF, calculated as the FT of the exit pupil wavefront. To include aberrations, the wavefront is mapped by a grid of rays, which are traced through the system.

In beam-propagation methods, the FT description is extended to deal with more general diffraction analyses, in particular those at nonimage planes where the FT method cannot be applied. At any chosen plane in the system, the wavefront is described in terms of a numerical 2-D distribution of complex amplitude. This distribution gives sufficient information to determine how the energy propagates on to the next analysis plane. Two methods are used in optical design software:

1. Analysis of the distribution into an angular spectrum, i.e., representing the field as a superposition of plane waves. This is incorporated in the software package[22] GLAD™ (generalized laser analysis & design).
2. A "decomposition" of the distribution into an array of beams (typically Hermite Gaussian modes[23]), equivalent to the so called "Gabor representation" of the field.[24] This type of analysis is incorporated in the software package[25,26] ASAP© (Advanced Systems Analysis Program).

In each case, the resulting wave or beam modes form a coherent set such that when they are superimposed, they reconstruct the wavefront. The onward propagation of the individual modes, to a chosen plane, can then be calculated, and so the wavefront can be reconstructed at that plane. In this way, the beam-propagation methods enable diffraction analysis to be made throughout the system by analyzing the wavefront at certain key points, for example, where the wavefront is "clipped" by apertures, where it is transformed by components, and finally at the plane where it is detected.

The result is a quite general and powerful tool for analysis of optical energy at any point in a complex system, in the presence of real aberrations. This finds use in, for example, laser beam propagation, nonimaging optics, and spatial filtering problems.

As well as being able to describe pupil-plane diffraction, as in the normal PSF computation, the beam propagation technique can describe diffraction occurring near an image plane (as, for example, at the field stop in the Lyot-stop problem). This type of diffraction has been analyzed using the beam-mode method of the ASAP program, in the context of diffraction effects from a spectrometer slit aperture.[27] In this program, the propagation algorithm is incorporated into a ray-trace program and this makes it readily applicable to real systems of complex geometry.

The beam-mode method is also used here for a full analysis of the Lyot-stop system. The incoming wave at the entrance aperture is decomposed to Gaussian beams, which are traced to the first image plane. From these beams, the optical energy over the field stop region is calculated. The resulting diffraction pattern, as spatially filtered by the field stop, is then decomposed into a new set of rays, and these are traced onward to the Lyot stop. This Gaussian beam decomposition and tracing is repeated, to describe the full diffraction patterns at each plane through the system, and examples of such an analysis are given in Sec. 4.

2.2.5 *Comparison of the PADE and beam-propagation techniques*

In comparison to the PADE method, the main advantage of beam propagation is that the full diffraction patterns can be calculated, including the central energy lobe. This also has the advantage of leading to greater physical insight, which is important in cases where aberrations or complex geometry are important, for example, where the stops cannot be placed at the ideal positions in the system, or where the design cannot be made to be well baffled.

The beam-propagation method enables great scope for detailed description of the diffraction processes in a Lyot-stop system, and the price paid for this is that often considerable computation is required. This is so for the same reason as in the FT method; the diffraction pattern at large off-axis angles involves high spatial frequencies (the wings of the PSF), and to describe these a corresponding fine grid resolution is required in the wave decomposition, leading to very large numbers of rays and points to be analyzed. In the Lyot-stop problem, the size of the computation is further increased, because the analysis must be repeated at multiple planes, and because in the ray trace, the number of quantities calculated for each ray is larger than in simpler programs. However, these considerations are becoming less important due to the continuing increases in readily available computer power.

For analysis of well-baffled Lyot-stop systems the beam-propagation technique is unattractive in relation to the PADE technique because, for this case, a full diffraction computation is relatively wasteful, since most of the diffraction pattern is not important, being blocked by the stops. The PADE technique is more efficient in this case since it selects only the ray paths that are not blocked, but that dominate the residual diffraction level at the detector.

The preceding differences between PADE and the beam-propagation methods mean that they find application in different aspects of diffracted-stray-light analysis for a typical instrument. For example, the PADE program is the choice for large-angle effects, as occur at the front end of the instrument where the range of off-axis source angles is large. Here the stray-light characterization involves repeating the computation over the full range of off-axis source angles (in limb viewing, for example, over the relevant part of the earth's disk). In this case, the beam-propagation computation would probably be impractically large, although it is useful for "spot checks" of energy patterns at particular angles of interest.

For narrower angle effects, as occur in later imaging stages of limb-viewing radiometers, the beam-propagation method becomes the more suitable choice. This is because, as we see in the next section, very small off-axis angles (<0.2 deg) become important, as do more of the fine detail of the optics, such as aberrations and resolution effects. There is the need to place stops at nonideal positions, and yet to defend against diffraction in the presence of pupil aberrations and over large wavelength ranges. We next de-

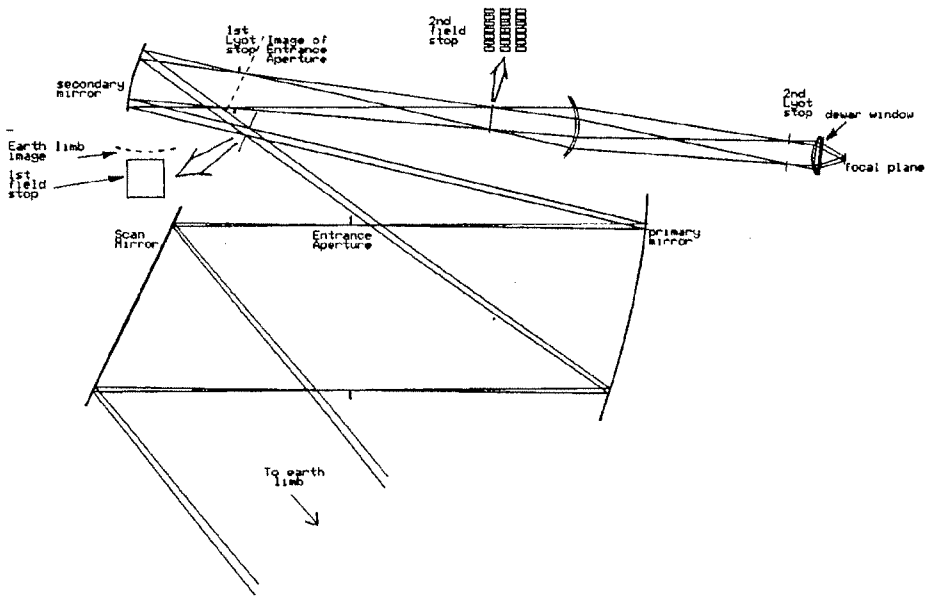

Fig. 5 Earth limb viewing radiometer, example optical design (HIRDLS instrument[23]).

scribe these issues with reference to current systems and show how they can result in the need for nonstandard Lyot-stop designs, which can be analyzed only using beam-propagation methods.

3 Applications in Design of Limb-Viewing Radiometers

Here we consider the typical design features of IR limb-viewing radiometers, with particular regard to the issues involved in aperture design for stray-light rejection. The signals to be detected are typically emission spectra,[4–8] in the wavelength region of approximately 6 to 17 μm, from thermally excited molecular vibration transitions in various species of trace gases in the atmosphere. A common feature in such instruments is the need to maintain high spatial resolution in the vertical direction (of the order of a few kilometers) to study small-vertical-scale chemistry of the atmosphere.

For a low-earth-orbit instrument, the distance to the earth limb is approximately $L = 3000$ km. The instrument aperture size is limited to typically $D = 200$ mm, and for this combination the diffraction limited Airy disk diameter d, using Eq. (3), is given as

$$d = 2.44 \frac{\lambda}{D} L.$$

At the longer wavelength region of $\lambda \approx 15$ μm, this gives $d = 0.55$ km. Therefore to obtain spatial resolution of the order of a few kilometers at the longer wavelengths of operation, this parameter can be only a few times larger than that in the diffraction-limited case.

3.1 *Telescope Design and Diffraction Control*

An example limb-viewing radiometer optical system is shown in Fig. 5, and this is the design for an instrument known as the High Resolution Dynamics Limb Sounder[6] (HIRDLS). A scan mirror steers the field of view such that the atmosphere is scanned vertically, from typically 10- to 100-km altitude, and also horizontally, over a larger range. The scan may also include views into a blackbody reference source, and/or cold space, to enable in-flight calibration of the detectors.

The telescope typically has a first imaging stage that is all-reflective. This helps to minimize scatter, and an off-axis unobscured design serves to minimize diffraction.[3] At the first image plane, a field stop is used to block the out-of-field radiances at the earliest opportunity. The example system in Fig. 5 is a Gregorian design in a z configuration, providing an accessible image plane between the primary and secondary mirrors. The first field stop is placed here, and as shown, this is rectangular, with the bright image of the earth horizon lying along one edge of the rectangle. This arrangement enables the earth to be blocked by positioning it just outside of the field of view, while viewing the wanted radiance from the atmosphere. In this way, the atmosphere can be viewed to low altitude without corruption of the signals by earth light. This feature is so important that in one instrument the aberration of the telescope is optimized for this imaging of the earth near the edge of the field of view, rather than for the signal near the center of the field, and this is so as to provide maximum blocking of the earth radiance.[5]

For the implementation of a Lyot-stop system in the telescope, there are usually several possible arrangements for the stop positions, with the exact choice being constrained by the particular beam folding of the off-axis design. In the example of Fig. 5 with Gregorian design plus

scan mirror, an EA can be accommodated between the scan and primary mirrors, such that it is imaged by the telescope to a position after the secondary, where there is space for a Lyot stop to be placed. The EA is positioned perpendicular to the optical axis, and with the off-axis pupil imaging, the subsequent image of the EA is then not perpendicular to the local optical axis, but is tilted, as shown. For reasons of accommodation, however, and for subsequent stop imaging, it is desirable to place the Lyot stop not in this ideal image plane, but instead in a plane perpendicular to the optical axis. To gain insight into the design trade-offs and performance of such a Lyot stop, detailed knowledge of the diffraction energy patterns in this region is required. For this, a method of generalized diffraction analysis at nonimage planes is needed.

The first Lyot-stop stage needs to block light that has been diffracted from outside of the telescope field of view, and this is made up of radiance from the earth disk and from the instrument's internal baffle structure. Without the Lyot stop, this diffraction can exceed the level of the required signal by several orders of magnitude; to eliminate this, the Lyot stop is required to have a similarly high blocking ratio R. It is found that even for a nonstandard Lyot-stop implementation, as in Fig. 5, such a requirement can typically be met within an acceptable range of Lyot-stop undersize factor of $a/r < 5\%$.

With blocking to such high levels, the first-stage Lyot-stop system can then be considered as well baffled. Another criterion to ensure this condition is that all front-end apertures ahead of the EA, for example, on the scan mirror and the instrument sun shade, are oversized sufficiently to ensure that their contribution to the diffracted stray light is negligible.

With such a well-baffled telescope system for the final diffraction performance characterization, the technique of the PADE program is appropriate, as explained in Sec. 2.2.5.

3.2 *Reimaging Systems*

Typically the first imaging stage is followed by reimaging or relay optics to accommodate the required detection systems. Examples include systems for radiometry and spectrometry, using grating, interferometer or dichroic filter devices,[4–8,28,29] and these can be of more than one type within the same instrument.[3,28] Such systems may share the instrument field of view, by this being subdivided, for example, using a second field stop, which has multiple apertures.[3,7,28]

In addition, each detection system may have multiple channels, typically to detect different atmosphere gas species by use of appropriate spectral range and resolution. The spectral requirements determine the type of spectrometer systems and the grouping of channels within each system. The division into spectral channels can be made by using mechanical interchange of spectral elements,[5] fixed dichroic beamsplitters,[8] or detector arrays with spectral filters such that each detector is assigned to one wavelength channel.[30] The array format may also be needed to obtain the required radiometric data; for example, to achieve the field coverage at an acceptable sampling rate and scanner speed. For the array format within one detection system, the division into channels leads to a further subaperturing of the field of view.

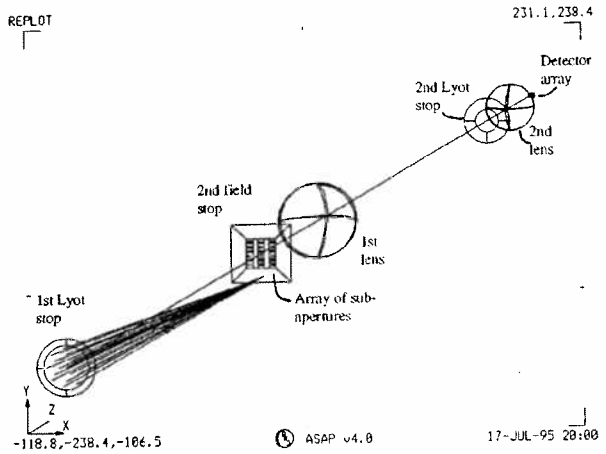

Fig. 6 Oblique view of reimaging system of Fig. 5, showing stop geometry and an example ray trace of an off-axis beam.

A feature that the preceding types of instrument have in common is that the first field defines a "composite" field of view, made up of the individual fields of view of the subsequent systems and/or channels of the instrument. The required subdivision of the field of view is made at subsequent field stops in the reimaging stages, and here detailed design of the apertures is needed to give the required stray-light defense within the constraints on system format and accommodation.

In the reimaging stages of an instrument, the required amount of stray-light rejection is less than in the first imaging stage, because the angular range of unwanted radiance is more restricted, thanks to the first field stop. Also, the sources of contamination are restricted by this stop and its surrounding enclosure. This means there is greater freedom in the use of component and material types. Typically a number of refractive optics and fold mirrors are used to give the required beam manipulation and accommodation of spectral components, while maintaining the image quality to be nearly diffraction limited, and with sufficiently low levels of stray light.

The example in Fig. 5 shows the case of field segmenting into a rectangular array of channels, which all pass through the same lens reimaging system in parallel for use with a detector array.[5,30] Figure 6 shows an isometric view of the reimaging system, where, at the second field stop, the field of view is split by a rectangular array of subapertures, and the subsequent reimaging is onto a corresponding array of detectors.[30]

Regarding stray-light control, the splitting of the field of view into subapertures is generally best made at the earliest opportunity, i.e., at the image plane after the telescope, to minimize scatter, ghost reflections, and diffraction effects. This is for similar reasons as in the telescope; by blocking the out-of-field radiances at the earliest opportunity, its scatter, or ghost reflection, in the subsequent optics is minimized. The image and field stop geometry of the system in Fig. 5 is shown in detail in Fig. 7 in terms of object space, i.e., equivalent dimensions at the earth's limb and neglect-

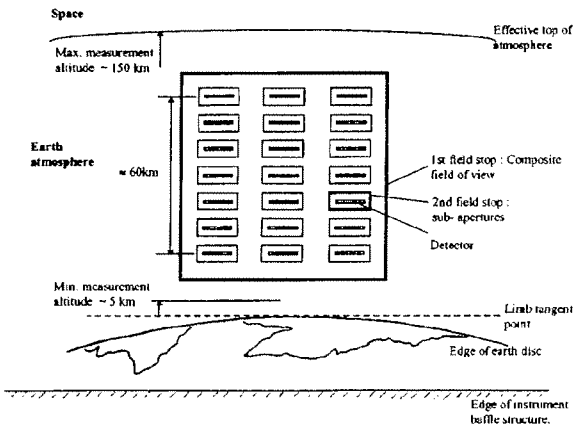

Fig. 7 Detector array and field stop configuration projected onto the earth limb (neglecting aberrations); 1 km is equivalent to 0.02 deg.

ing system aberrations. The first field stop defines a single rectangular region, this being the composite field of view. At the second field stop, an array of rectangular apertures define each channel field of view within the composite field. The final field stop is at the detectors, and this is a mask defining the detector fields of view as the rectangular strips of atmosphere to be sensed. As shown, these are undersized with respect to the second field stop. The relative sizing of the consecutive field stops is to progressively cut down the out-of-field region and to minimize the effect of stray light generated at aperture edges, as explained later in Sec. 3.2.1.

In Fig. 7, the out-of-field radiances are those coming from the parts of the composite field other than that of the channel being considered, and the stray light in this case would appear as crosstalk between channels. To remove the crosstalk effect, the subdivision of the field of view must often be not just spatial (i.e., by means of the mask type aperture) but also spectral (i.e., the subapertures at the second field stop should each include a spectrally selective filter) so that the radiometric path to the channel detector is uniquely defined at the earliest possible point.

This issue of crosstalk within a composite field of view is important in this type of instrument because the composite field of view may need to cover a large vertical portion of the atmosphere, of size[5,6] typically >50 km, and over such an altitude range the brightness of the earth's atmosphere can vary by approximately two orders of magnitude, due to the decrease in temperature and concentration of gases with increasing altitude. The result is that measurements of very faint radiances near the top of the atmosphere may be corrupted by the bright radiances near the bottom of the atmosphere, arriving via the stray-light mechanisms described. Also, in some measurements where the channels near the top of the array in Fig. 7 are to view the lower altitudes of the atmosphere, part of the composite field of view lies on the earth disk such that the bright earth radiance actually penetrates the first field stop, and this presents a particularly severe stray-light problem.

The preceding discussion is to highlight the areas of instrument design that are sensitive to stray-light effects. We next consider the stray-light effects themselves and the measures that can be taken for their reduction when designing aperture systems.

3.2.1 *Scatter*

The scattered stray light in the reimaging stages arises when light from one part of the composite field of view is scattered by surface or edge imperfections in the components into another part of the field of view, occupied by a different channel. Surface imperfections are due to

1. residual roughness left after manufacture of the lenses and filters, which affects the choice of materials and fabrication techniques
2. particulate contamination, occurring during instrument building and testing, and during flight.

Since scattered intensity is smaller at larger scatter angles, the effect can be reduced by having the channel fields of view well separated within the composite field of view.

Stray light generated at the edges of the field stop apertures by edge scatter and diffraction[15] can also be reduced by separating the fields of view. This gives room for the detectors to be undersized with respect to the previous field stop apertures (as in Fig. 7). The edge-generated stray light imaged from the edge of the field stop to the detector plane is focused there to produce a bright line at the image of the field stop edge. With the undersizing, this imaged stray light falls outside the detector area and it is not detected.

These scatter considerations imply channel fields of view well separated in the composite field, but the disadvantage is that this creates more unused "dead space" in the field coverage. This may, however, be filled by the scanning function of the instrument.

3.2.2 *Ghost reflections*

Lens-based imaging leads to ghost reflection effects, particularly for instruments in which each channel in the composite field of view is for a different wavelength of signal. In the array detector re-imaging system of Fig. 6, for example, light from one position within the composite field of view is incident on the detector filter of channel A and is spectrally out of band. It is therefore reflected back into the lens system, where it is partially rereflected at the lens surfaces and returned to the detector array (as a defocused beam). If it were then incident on the filter of a different channel B, for which it is spectrally in band, it would produce a ghost signal, originating from the wrong field position, that of channel A. The ghosting thereby produces spurious crosstalk between channels. Unlike the scatter case, the size of the ghost levels does not always decrease with increasing angular separation of channels within the composite field of view. The ghost levels depend on the lens system design, and they can be calculated by means of ray-trace analysis. The problem is significant in this type of instrument because the systems are often required to cover a wide wavelength range (the wavelength variation between channels can be[7,8,30] by a factor of greater than 3), and this limits the efficiency that can be obtained in the antireflection coatings on the lens surfaces.

The main method for reducing this problem is the placement of spectral filters at the point where the composite field of view is first divided into channels. In the example

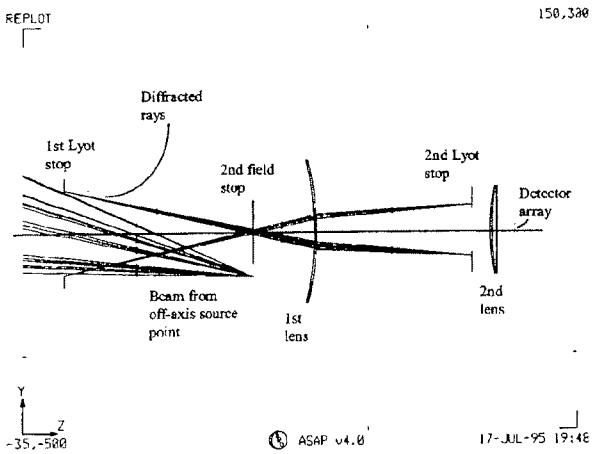

Fig. 8 Second Lyot-stop stage of Fig. 5 expanded vertically to show ray-trace detail. Traced rays are for an off-axis beam, blocked at the second field stop, and for the resulting diffraction from the first Lyot-stop edge, blocked at the second Lyot stop. For clarity, not all of the traced rays are plotted.

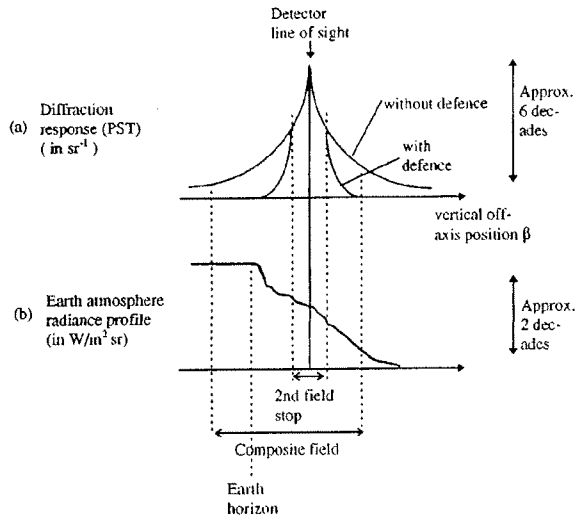

Fig. 9 (a) Example instrument diffraction response (PST), showing effect of a possible defense by the second Lyot stop. For quantitative plot see Fig. 13. (b) Example earth atmosphere radiance profile.

of Fig. 5, this involves an array of filters at the second field stop, i.e., in front of the lens reimaging stage, restricting the out-of-band light incident on the lenses.[30] In another example, mechanically interchangeable filters are placed ahead of the lenses so that only one wavelength at a time is permitted through the lens system.[5]

3.2.3 *Diffraction*

In the reimaging stage, the same diffraction design principles apply as in the telescope stage, and it is usually possible for a second stage of Lyot stop to be implemented. For the example system, the reimaging stage with Lyot stop is shown in Fig. 8. The source of diffraction for this second stage is the aperture of the first Lyot stop, since by virtue of its undersizing, this becomes the new beam-defining aperture for the reimaging stage, and it thereby generates a new set of diffracted rays, shown in the figure. The first lens images the first Lyot stop to a position in front of the final focusing lens, and here a second Lyot stop is introduced. The second Lyot stop is undersized with respect to the first, and since it is also the last stop in the system, it becomes the system aperture stop. The main difference from the diffraction at the entrance aperture is that, as for scatter, the range of out-of-field angles is in this case much smaller, being restricted to the field of view defined by the first field stop.

In instruments where no subaperturing of the field of view is made prior to the reimaging stages, the F-number and stop radius of the Lyot stop system are usually not greatly different from those of the telescope stage, and this enables high blocking levels to be obtained in the second Lyot-stop stage similar to those in the first. The resulting combination of two "cascaded" stages of efficient Lyot stops has been used in this case to obtain net diffraction blocking to very high levels.[5]

In instruments with subdivision of the field stop, however, the efficiency of the second Lyot stop stage is reduced as follows. The field of view for any one channel is reduced by the subaperturing, and for the rays diffracted by the first Lyot stop, this limits the angular size of the cone of rays transmitted to the second Lyot stop. The F-number of the diffracted beams is increased, and therefore so is the width b of the bright ring of diffracted light [Fig. 1 and Eq. (1)]. That is, the reduced field stop produces a loss of resolution in the imaging of the diffracted rays from the first to the second Lyot stops.

This loss of resolution is significant in instruments that have many channels. If, for example, the composite field of view (FOV) size were split into $N \times N$ equal subapertures, with negligible spacing between channels, then b would be increased by a factor N as compared to the case without subaperturing. In Fig. 6, for example, $N=7$ in the vertical direction, and as a result we no longer have $b \ll r$, and the diffraction image can then not be blocked effectively without an excessively large loss of throughput. A well-baffled defense is then no longer possible.

The segmentation of the second field stop into smaller channel field stops does, however, also provide an opportunity for defense against narrow-angle diffraction from within the composite FOV. If we consider a single channel with the subapertures present at the second field stop, most of the light from the parts of the object scene not intended to be recorded by any detector is blocked at the second field stop, and consequently the diffraction of this light (from the first Lyot stop) can be defended against using the second Lyot-stop stage, albeit with the limited efficiency already described. No such defense is possible in instruments that do not have this segmented second field stop, since then all of the composite FOV light is instead transmitted and imaged directly on to the detector plane.

Figure 9 illustrates this diffraction defense situation. Figure 9(a) shows the PST response for one detector in the vertical direction for the cases with and without the second Lyot stop present. Figure 9(b) shows the typical source radiance distribution at corresponding altitudes in the

earth's atmosphere. With no second stage Lyot stop, the PST falls as 1/(off-axis position)^3 [Eq. (6)], but with the Lyot stop system added, for off-axis positions beyond the second field stop edge [$\beta > \delta$ in Eq. (9)], additional defense is obtained (decreasing the PST). The figure also shows how, for off-axis positions close to this edge, the PST increases asymptotically toward the edge, as given by Eq. (9) with $\beta \rightarrow \delta$. The appearance of Fig. 9(a) might at first suggest that the PST suppression is due simply to the blocking action of the second field stop. However, this diffraction suppression is not obtained by the presence of the field stop subaperture alone, but requires the presence of both this aperture and the second Lyot stop, as explained in Sec. 2.2.2.

The PST plot can be interpreted as a plot of detector sensitivity to different portions of the scene, although it should not be mistaken for a plot of actual energy at the detector plane. The net stray light level B_{stray} (described in terms of equivalent radiance incident on the instrument) is given by the BDDF multiplied by the scene radiance B_{scene} and integrated. Using Eq. (5) to convert BDDF to PST, this gives

$$B_{\text{stray}} = \frac{4F^2}{\pi} \int_{\Omega} B_{\text{scene}}(\beta)\,\text{PST}(\beta)\,\text{d}\Omega. \tag{10}$$

The integration is in two dimensions over the solid angle Ω of the composite field of view, and it can be seen that the integrand is the product of the distributions in Figs. 9(a) and 9(b).

Figure 9 shows how the second Lyot stop stage effectively sharpens the system response function by suppressing the wings of the PST. Although this can help to reduce the channel crosstalk problem, this effect is not as important in the case of diffraction as it is for scatter and ghosting, since for diffraction, the PST fall-off with angle is in any case relatively rapid, even before the second Lyot-stop stage is applied. A more important effect for diffraction is that of very narrow angle stray light from regions close to the channel field of view. In limb-viewing radiometers, the defense of this region is particularly useful for the following reasons:

1. Often all of the channels are required to view to low altitude ($\sim$10 km), where the bright earth disk not only penetrates the first Lyot-stop stage but is also very close to the channel field of view ($\sim$0.2 deg). It therefore requires the best possible narrow-angle rejection by the second Lyot-stop stage.
2. The net instrument response is required to be of best possible vertical resolution; and at the wavelengths used, this is limited by diffraction.

Because of the relative inefficiency of the second-stage Lyot stop, when subapertures are used at the intermediate field stop, the trade-off between the amount of diffraction suppression, and the amount of throughput obtained, must be analyzed in detail. The inefficiency of the blocking and the narrow diffraction angles involved (system not well baffled), mean that the most generalized diffraction model, that of Gaussian beam superposition, must be used, and an example of such an analysis is presented in the next section. While this example shows the application of a powerful analysis method to one particular instrument, the technique is applicable to other optical systems, both limb viewing and of other types.

4 Design Study for a Nonstandard Lyot Stop

In this section the beam propagation method is applied, to the radiometer design[30] of Figs. 5 and 6 using the ASAP© program. This is to model the second Lyot-stop stage, to quantify the departure from the ideal case, and illustrate the design trade-offs. Figure 8 shows the reimaging stage of the instrument in a vertical section view corresponding to the oblique view of Fig. 6. Only one channel is to be considered here; the on-axis channel, i.e., the central detector in the array. The center wavelength of this channel is 16.5 μm.

In constructing the beam-propagation analysis it is useful to first compute a test case, to check the accuracy of the numerical representation. For simplicity we use a 1-D case, taking all apertures to be rectangular, with dimensions in the y direction as given in Fig. 8, but with infinite extent in the plane perpendicular to that of the diagram. Also, the analysis is for a single position of the off-axis point source. The first Lyot stop then behaves as a slit aperture, and its diffraction pattern at the second field stop would be given by a 1-D sinc function in the y direction, rather than the 2-D Airy function of Sec. 2. A further assumption is that the off-axis angle β is large, such that in the region of the field stop the sinc function approximates to a sine function.

In the boundary-wave formulation of Sec. 2, this is equivalent to the pattern being dominated by the diffracted rays, as shown in Fig. 8, emanating from each side of the first Lyot stop, with angular range set by one of the apertures of the second field stop. To model this system the two sets of diffracted rays are simulated as coherent line sources, and their propagation on to the field stop is modeled. The resulting optical intensity pattern at the field stop is shown in Fig. 10(a) in vertical section. This has the expected sinusoidal fringe structure (as in the Young's slit experiment[31]), since the diffracting edges in Fig. 8 are modeled as two line sources. The pattern has boundaries defined by the field stop aperture.

To simulate the onward propagation, the fringe pattern is then decomposed into a new set of beam modes, which are traced onward to the second Lyot stop. The energy pattern analyzed at this plane is shown in Fig. 10(b). This has the form of two energy lobes, and these are found to be correctly centered at the images of the two edges of the first Lyot stop. Since the fringe intensity envelope at the field stop is a 1-D "top-hat" function [Fig. 10(a)], according to Fourier optics, the shape of each lobe at the Lyot stop should be a sinc function, representing the diffraction blur for the imaging of the first Lyot stop, through the field stop, onto the second Lyot stop. The width of the main energy lobes in Fig. 10(b) is found to agree with the predicted blur diameter $b = 2.6$ mm [Eq. (1)]. This test case was used in constructing the computer model, to ensure that enough beam modes are present to model the diffraction patterns with sufficient numerical accuracy.

Having checked the model against a known result from Fourier optics, to demonstrate its generality, the energy pat-

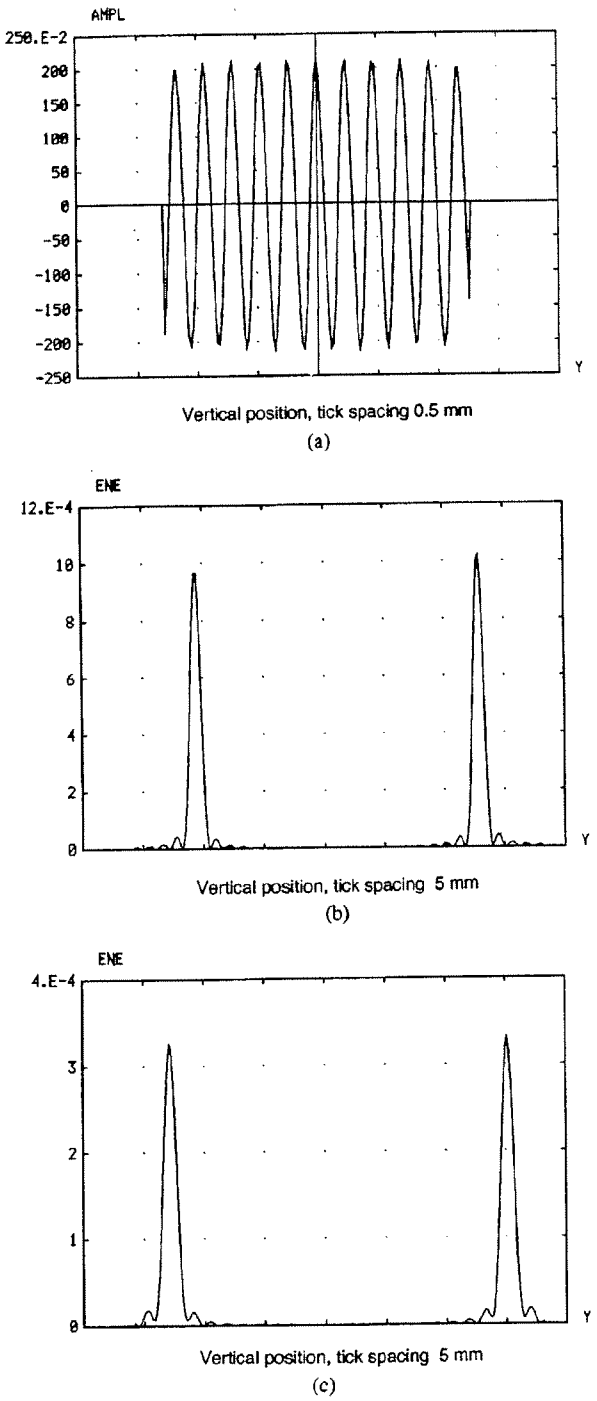

Fig. 10 Computed energy patterns for approximated model (Young's slit apertures): (a) at second field stop, shown in terms of electric field amplitude; (b) at second Lyot stop, shown in terms of energy; and (c) at defocused position, 50 mm behind second Lyot stop.

tern at an arbitrary plane is computed. Figure 10(c) shows the pattern at a position 50 mm behind the second Lyot stop. Comparison with Fig. 10(b) shows how the diffraction pattern is defocused and widened slightly. (The defocus distance chosen here has to be relatively large, to make the effect evident at the relatively low divergence of the diffracted rays in this case). This type of computation is useful for Lyot-stop design in situations where the stop cannot be placed at the ideal image location, but must instead be defocused or tilted, e.g., for accommodation reasons.

Next the analysis for the real 2-D apertures of Fig. 6 is given. Because the first Lyot stop is circular, the pattern at the second field stop is a 2-D Airy ring pattern rather than the 1-D sine function of Fig. 10(a). To include the system optical aberrations, the model generates this pattern using a ray trace of the off-axis beam cone, as shown in Figs. 6 and 8.

Figure 11(a) is a vertical cross section of the resulting diffraction pattern at the field stop (with the energy plotted on a log scale). Here the point at which the energy is a maximum is the center of the PSF; i.e., the point in Fig. 8 where the off-axis beam is focused. In this example, the off-axis point is that corresponding to the minimum off-axis earth distance during viewing, i.e., the minimum measurement altitude, which is 8 km in this case. The figure also shows the Airy ring intensity falling as $1/(\text{angle})^3$ [Eq. 6] and extending across the field stop aperture of the channel under consideration, where it is shown as the solid line. Only this part of the pattern is transmitted by the field stop. Its onward propagation is analyzed as previously, and the energy pattern at the second Lyot stop is shown in Fig. 11(b) in vertical section. In comparison to the approximated case of Fig. 10(b), there is some additional widening of the energy lobe due to the $1/(\text{angle})^3$ decay of the diffraction PST in this case, and this further reduces the efficiency of the second Lyot stop.

Figures 12(a) and 12(b) give examples of the full 2-D diffraction patterns at the same stop positions as in Figs. 11(a) and 11(b), and these patterns are actual computations of the types of pattern depicted schematically in Fig. 4 earlier. Figure 12(a) is the spatially filtered Airy ring pattern, and Fig. 12(b) shows how this results in a partial bright ring at the image of the diffracting aperture. This image has greatest intensity at the top and bottom of the ring, and this is because the off-axis earth point chosen [marked in Fig. 12(a)] is off-axis in the vertical direction. Since the net energy pattern at the second Lyot stop would be the sum of patterns over all relevant field points, the ring image will "fill out" into a more uniform ring, as points with some horizontal off-axis displacement are included. Nevertheless, because the main off-axis source is the earth disk, displaced vertically with respect to the instrument line of sight (Fig. 6), the net ring pattern will still be at its brightest in the vertical direction, as in Fig. 12(b). This feature could lead to the consideration of elliptical Lyot stops for limb viewing; i.e., one with smaller diameter in the vertical direction, where most of the diffracted energy lies. Such a stop would minimize the loss of throughput involved in implementing a given amount of diffraction blocking.

For simplicity, in this example, we consider a circular Lyot stop with an undersize of 6% with respect to the diffraction image, and this is shown in Fig. 12(b). This is one possible value for the trade-off between diffraction defense needs and the resulting loss of throughput (the latter scales as the square of the stop diameter).

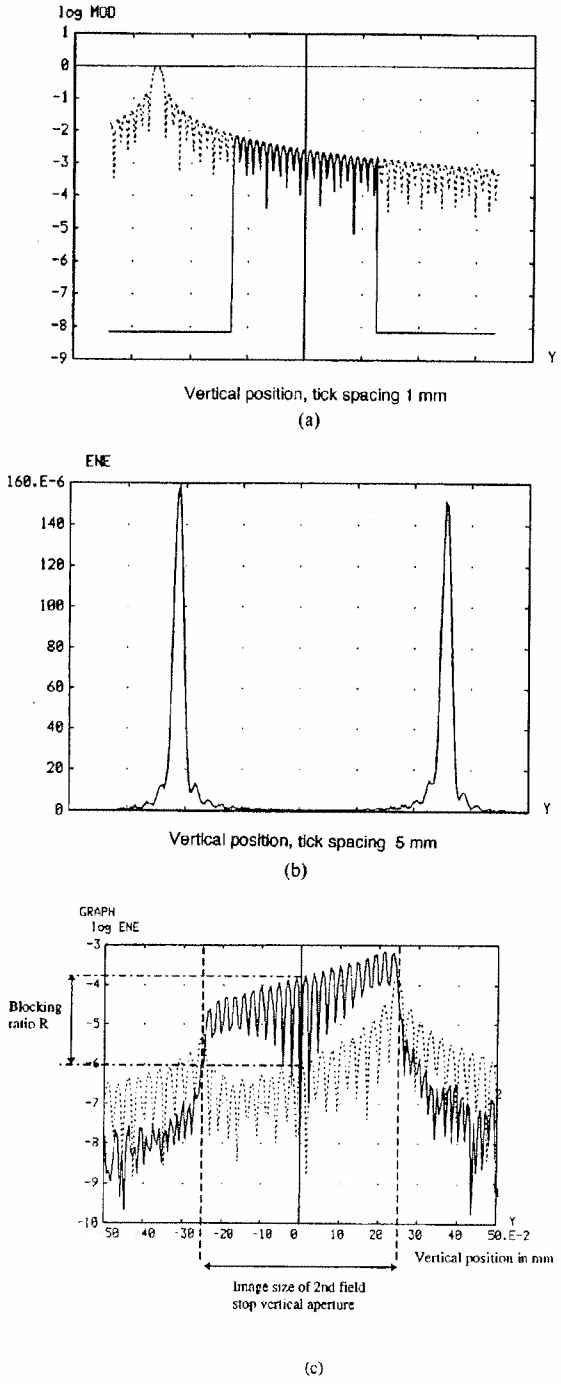

Fig. 11 Computed energy patterns for full diffraction model of real apertures of Fig. 8 shown in vertical section: (a) second field stop, Airy ring pattern (dotted line) and portion transmitted by the stop (solid line); (b) second Lyot stop plane; and (c) final image plane, solid line is for normal imaging of the pattern of (a) (no Lyot stop) and dotted line is diffraction remnant with Lyot stop applied.

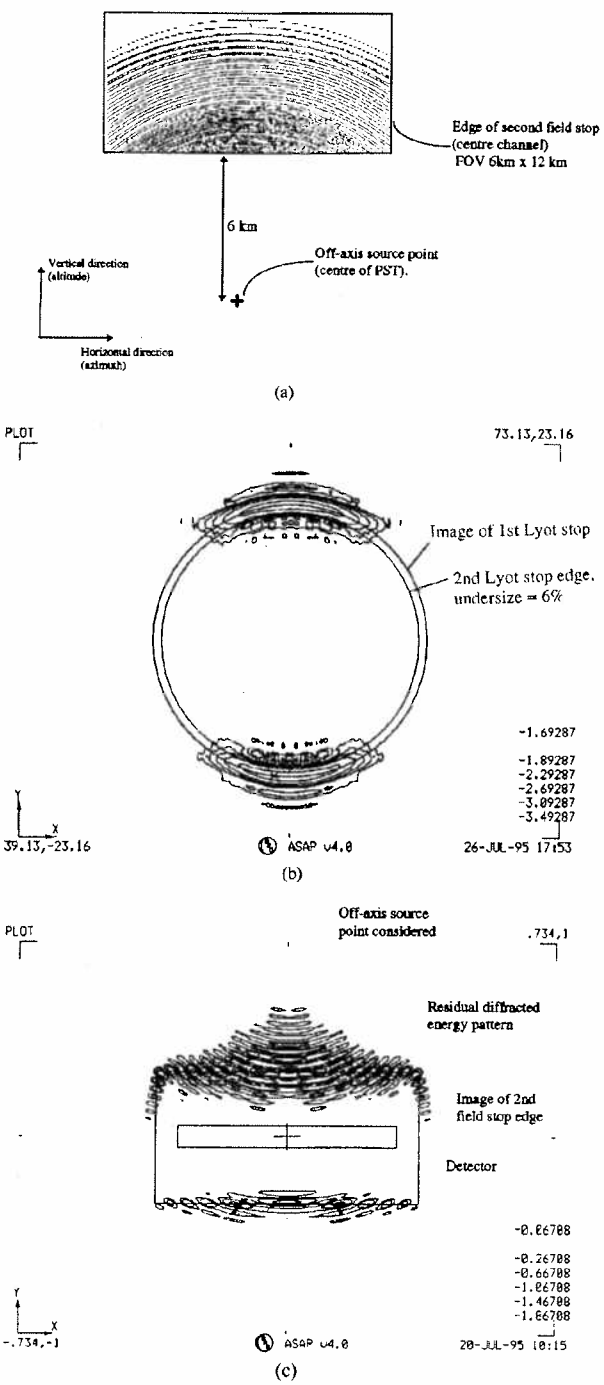

Fig. 12 Full 2-D energy patterns (of which Fig. 11 are vertical sections) shown in relation to aperture geometries: Contour plots (a) at second field stop (contours showing pattern shape only); (b) at second Lyot stop (contours on log scale, five levels, and peak level shown at bottom left); and (c) at final image plane [contours on log scale as in (b)].

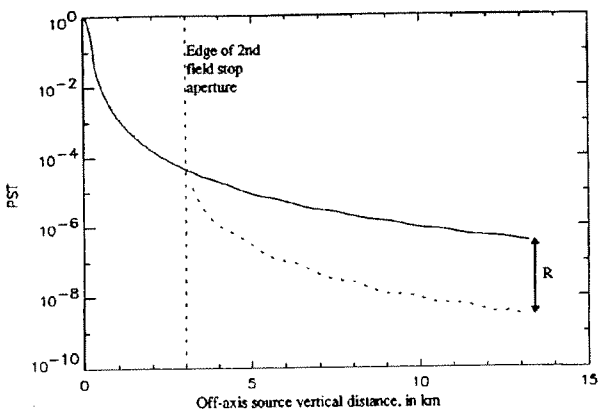

Fig. 13 Diffraction PST plotted versus off-axis source vertical position in kilometers; solid line is normal diffraction PST and dotted line is PST with the second Lyot-stop stage added.

In the diffraction computation, the energy pattern of Fig. 12(b) is spatially clipped by the Lyot stop, decomposed into beam modes, traced onward to the image plane, and reconstructed, to give the final diffraction pattern, shown in Figs. 11(c) and 12(c) in one and two dimensions, respectively. These patterns retain the Airy ring structure of the pattern at the previous field stop [Figs. 11(a) and 12(a)]. Indeed, in the absence of the second Lyot stop, the pattern at the image plane replicates the pattern at the previous field stop, actually being an inverted image of it. Figure 11(c) shows the vertical energy pattern, on a log scale, both with and without the Lyot stop present, to illustrate how the Lyot stop reduces the overall energy level. Also, the residual energy is greatest around the image of the field stop edge, and this property is also evident in the 2-D plot of Fig. 12(c). This effect is that discussed previously in Sec. 1 and Fig. 2, being the double-diffraction energy that, in the boundary wave formulation, originates by diffraction from the edge of the first field stop.

The detector aperture is also shown in Fig. 12(c), and the diffracted energy actually measured is only that part of the pattern that falls on the detector. This figure illustrates the importance of the oversizing of the second field stop with respect to the detector, such that the double-diffraction image falls well outside the detector. In Fig. 11(c), the detected energy level is marked for the cases both with and without the Lyot stop present, and the blocking ratio R of the Lyot stop is calculated as the ratio of these two energy levels. In the actual computation with finite detector size, the integral of energy over the detector area is used.

To construct the response function of the system with the Lyot stop, the preceding simulation and calculation of R is repeated over a range of off-axis angles. This gives the diffraction PST, and the results are plotted in Fig. 13 over the range 0 to 14 km from line of sight. This figure quantifies the behavior illustrated earlier in Fig. 9(a). The 3-km point is that equivalent to the second field stop half-aperture size, and so below this point the diffraction is undefended. At increasing off-axis angles >3 km, the Lyot stop becomes more efficient [R decreasing, as predicted by Eq. (9)], and R approaches a value of 10^{-2} at >10 km. This data shows that despite the nonideal geometry of this Lyot stop (6% undersize in radius compared to diffraction ring width of approximately 10%), and despite the narrow angle range and long wavelength, useful blocking of the diffracted light from the bright earth disk (present near 10 km) can be obtained.

The preceding analysis gives the response function for off-axis angles in the vertical direction only, and for a full analysis the computation would be repeated over the full 2-D range of off-axis angles β. To find the total amount of earth light incident on the detector, the net PST response would then be multiplied by the scene radiance, and integrated. This full analysis is evidently quite large, requiring many ray-trace and energy calculations. It may also need to be repeated for different channels and different viewing directions. Because the diffraction ring width at the second Lyot stop is proportional to the wavelength, it will vary between channels. Also, in some of the off-axis channels, there is significant aberration present in the imaging between pupil planes. These effects mean that the performance of the second Lyot stop will vary significantly between channels, and so several channels may need to be analyzed.

In practice, the analytical task can be reduced by identifying the few "worst-case" situations. For example, the diffraction performance is worst in the long-wavelength channels (the preceding example is one such channel), and the worst-case viewing geometries can also be identified. The results given here are intended as an example to illustrate the use of the beam-propagation technique for analysis of diffraction-dominated effects of this type.

5 Summary

A generalized diffraction analysis technique has been used to characterize the performance of a nonideal Lyot stop for suppression of narrow-angle diffraction, as required in an earth limb viewing radiometer.

The various Lyot stop analysis methods were reviewed in the context of limb-viewing instruments. The main modern methods for describing full instrument geometries are the PADE™ technique and the beam-propagation technique, as implemented in the GLAD™ and ASAP© programs. The issues involved in aperture design for multichannel instruments of this type were explained, and how these can lead to a requirement for nonstandard Lyot stops in the reimaging stages was shown. It was found that the most general and powerful technique, that of beam propagation, was required to adequately describe the diffraction defense in this type of Lyot-stop system.

Illustrations were given on how this method, by enabling full energy computations at any plane in the instrument, provides good physical insight into the diffraction process and the associated design trade-offs. An example analysis of a nonstandard second Lyot-stop stage for an example instrument design having a detector array format showed that even with a modest undersize of 6% (12% throughput loss), a significant amount of narrow angle blocking ($R \approx 10^{-2}$) was obtained. Thus although the need for subaperturing of the field of view prevents the implementation of an ideal or well-baffled Lyot stop, the nonideal alternative is shown to be still useful in providing significant narrow-angle earth disk rejection. It is therefore an important design feature, contributing to one of the major design aims in

this type of instrument; measurement of the atmosphere at high vertical resolution under severe stray-light conditions. Furthermore, it demonstrates that the design of such nonideal diffraction rejection systems can now be considered in real systems of arbitrarily complex geometry, thanks to the powerful optical analysis tools now available.

There are, of course, other optical design problems that require analysis of diffraction to a level of geometric detail and generality similar to that used here. These problems tend to be those involving relatively long wavelengths, ranging from IR to millimeter-wave optics. The need for analysis at arbitrary planes can arise for a variety of reasons. In this case, the reason is the nonideal geometric constraints, and other cases include those of diffraction patterns of similar size to components,[27] or the use of nonimaging optics. As well as use for diffraction stray light design, other fields of use are antenna design, laser cavity design, and beam-propagation problems.[22,25,32]

Although the formulation of such detailed optical analyses can be lengthy, they have been made practical by the large computer powers now available, along with the development of advanced ray-trace programs incorporating beam analysis methods. This enables powerful techniques, such as Gaussian beam superposition, to be readily combined with real system geometries, as modeled via other computer-aided engineering programs.

Acknowledgments

The work described here was undertaken as part of the instrument optical design and analysis for the HIRDLS project (High Resolution Dynamics Limb Sounder). The HIRDLS instrument is planned to fly on the EOS-CHEM satellite, currently scheduled for launch in 2002. This is a joint undertaking by a USA-UK team led jointly by principal investigators Dr. J. C. Gille from the National Center for Atmospheric Research and the University of Colorado, Boulder, Colorado, and Dr. J. J. Barnett from Oxford University, United Kingdom.

The authors acknowledge the financial support of the HIRDLS United Kingdom government funding body, the Natural Environment Research Council (NERC). Other acknowledgments are due to H. Morrow of the Lockheed-Martin Palo Alto Research Laboratory and M. Anapol of Sensor Systems Group Inc., for drawing the authors' attention to previously published work on the diffraction defense in previous telescopes of this type; R. Pfisterer and A. Greynolds of Breault Research Organisation, Inc., for tuition and advice in the use of the ASAP program; and I. Tosh, A. Richards, and A. Ridgeley of Rutherford Appleton Laboratory for advice and useful discussions on the optical design and stray-light design inputs concerning the HIRDLS instrument.

References

1. B. Lyot, "A study of the solar corona and prominences without eclipses," *Mon. Not. R. Astron. Soc.* **99**, 580–594 (1939).
2. J. B. Breckinridge, T. G. Kuper, and R. V. Shack, "Space telescope low-scattered-light camera: a model," *Opt. Eng.* **23**(6), 816–820 (1984).
3. M. I. Anapol and A. A. Mastandrea, "Design and fabrication of reflective optical systems for space and tactical flight applications," in *Reflective Optics II, Proc. SPIE* **1113**, 146–159 (1989).
4. J. C. Gille and J. M. Russell III, "The limb infrared monitor of the stratosphere: experiment description, performance and results," *J. Geophys. Res.* **89**, 5125–5140 (1984).
5. T. A. Birge, "Stray light analysis of the cryogenic limb array étalon spectrometer," in *Stray Radiation V, Proc. SPIE* **675**, 152–159 (1986).
6. J. C. Gille and J. J. Barnett, "Conceptual design of the high resolution dynamics limb sounder (HIRDLS) for the EOS chemistry mission," *Proc. SPIE* **2830**, 190–201 (1996).
7. F. W. Taylor, C. D. Rodgers, J. G. Whitney, S. T. Werrett, J. J. Barnett, G. D. Peskett, P. Venters, J. Ballard, C. W. P. Palwer, R. J. Knight, P. Morris, T. Nightingale, and A. Dudhia, "Remote sensing of atmospheric structure and composition by pressure modulator radiometry from space: the ISAMS experiment on UARS," *J. Geophys. Res.* **98**(D6), 10799–10814 (1993).
8. M. Endemann, G. Lange, and B. Fladt, "MIPAS (Michelson interferometer for passive atmosphere sounding) for Envisat-1," *Proc. SPIE* **2209**, 36–47 (1994).
9. J. J. Guregian, R. T. Benoit, and W. K. Wong, "An overview of contamination effects on the performance of high straylight rejection telescopes via ground measurements," in *Optical System Contamination: Effects, Measurement, Control II, Proc. SPIE* **1329**, 2–15 (1990).
10. A. Sommerfield, *Optics*, p. 249, Academic Press, New York (1954).
11. A. Rubinowicz, "The Miyamoto-Wolf diffraction wave," in *Progress in Optics*, Vol. IV, p. 205, J Wiley & Sons (1965).
12. W. J. Smith, Modern Optical Engineering, McGraw-Hill, 1990, p. 452.
13. R. J. Noll, "Reduction of diffraction by use of a Lyot stop," *J. Opt. Soc. Am.* **63**(11), 1399–1402 (1973).
14. A. W. Greynolds, "Formulas for estimating stray-radiation in well-baffled optical systems," in *Radiation Scattering in Optical Systems, Proc. SPIE* **257**, 39–49 (1980).
15. E. R. Freniere, R. D. Stern, and J. W. Howard, "SOAR: a program for the rapid calculation of stray light on the IBM PC," in *Stray Radiation in Optical Systems, Proc. SPIE* **1331**, 107–117 (1990).
16. J. W. Goodman, *Introduction to Fourier Optics*, McGraw-Hill, New York (1968).
17. H. H. Hopkins and M. J. Yzuel, "The computation of diffraction patterns in the presence of aberrations," *Opt. Acta* **17**(3), 157–182 (1970).
18. M. Born and E. Wolf, "The boundary diffraction wave," Chapter 8.9 in *Principles of Optics*, 6th ed., pp. 395–396, Pergamon Press (1986).
19. B. R. Johnson, "Analysis of diffraction reduction by use of a Lyot stop," *J. Opt. Soc. Am.* **4**(8), 1376–1384 (1987).
20. E. Hansen and W. L. Wolfe, "Baffling design of a three mirror off-axis celestial telescope," in *Infrared Technology XVII, Proc. SPIE* **1762**, 33–38 (1992).
21. A. W. Greynolds, "Method for calculating diffraction effects in optomechanical systems of arbitrary geometry," in *Radiation Scattering in Optical Systems, Proc. SPIE* **257**, 64–77 (1980).
22. "Generalised Laser Analysis & Design (GLAD™)," Applied Optics Research, Pittsford, NY (1996).
23. T. Tamir and H. Blok, Eds., "JOSA feature issue on propagation and scattering of beam-fields," *J. Opt. Soc. Am. A* **3**(4), 462–464 (1986).
24. P. D. Einziger, S. Raz, and M. Shapira, "Gabor representation and aperture theory," *J. Opt. Soc. Am. A* **3**(4), 508–522 (1986).
25. A. W. Greynolds, "Propagation of generally astigmatic gaussian beams along skew ray paths," in *Diffraction Phenomena in Optical Engineering Applications, Proc. SPIE* **560**, 33–50 (1985).
26. "Advanced Systems Analysis Program (ASAP©)," Version 4.0, Publ. Breault Research Org. Inc. 6400 East Grant Road, Tucson, AZ (1995).
27. M. Satter, "Computer modelling of slit diffraction (spatial filtering)," in *Stray Radiation in Optical Systems II, Proc. SPIE* **1753**, 105–114 (1992).
28. A. A. Mastandrea, R. T. Benoit, and R. R. Glasheen, "Cryogenic testing of reflective optical components and telescope systems," *Proc. SPIE* **1113**, 249–256 (1989).
29. J. S. Titus and D. Wang, "Cryogenic infrared radiance instrument for shuttle (CIRRIS) telescope," *Opt. Eng.* **23**(3), 319–322 (1984).
30. R. Hunneman, J. J. Barnett, and G. J. Hawkins, "High-performance infrared filters for the HIRDLS channel focal plane detector array," *Proc. SPIE* **2210**, 516–532 (1994).
31. E. Hecht and A. Zajac, *Optics*, 6th ed., pp. 281–283, Pergamon Press, New York (1986).
32. M. Caldwell, P. F. Gray, and P. McNamara, "Computer-aided modeling of beam propagation effects in diffraction-critical spaceborne instruments," *Proc. SPIE* **2774**, 75–88 (1996).

Martin E. Caldwell received a BA in physics in 1987 from the University of Cambridge, an MPhil in 1989 for research in photodetector devices from the University of Sheffield, and a PhD in 1991 for research in spatial light modulators from Imperial College, London. He subsequently was an optical engineer at the GEC Marconi Research Centre, Chelmsford, working on coherent laser radar systems for wind speed measurement. Since 1994 he has been an optical system scientist at the Rutherford Appleton Laboratory, working on a variety of optical instruments, mainly for space-borne remote sensing and astronomy applications.

Peter F. Gray received a BSc degree (hons.) in applied physics from Brighton College of Technology, England, in 1970 and MSc and PhD degrees in applied optics from Imperial College, London. After 3 years as a postdoctoral research associate in the Applied Optics Group at Imperial College, he worked on the development of manufacturing techniques for optical components in the optical industry, at Grubb Parsons, Newcastle upon Tyne, England. He joined the Space Science Department of Rutherford Appleton Laboratory in 1980, where he has carried out design, analysis, and alignment on optical systems for a wide variety of space satellite instruments for earth observation and astronomy. He currently leads the Optical Systems Group in the Space Science Department at Rutherford Appleton Laboratory.